RSC Advances

PAPER

View Article Online
View Journal | View Issue

Cite this: *RSC Adv.*, 2021, **11**, 20151

Two novel oxetane containing lignans and a new megastigmane from *Paronychia arabica* and *in silico* analysis of them as prospective SARS-CoV-2 inhibitors†

Abdelsamed I. Elshamy,[ab] Tarik A. Mohamed,[c] Mahmoud A. A. Ibrahim,[d] Mohamed A. M. Atia,[e] Tatsuro Yoneyama,[a] Akemi Umeyama[a] and Mohamed-Elamir F. Hegazy *[cf]

The chemical characterization of the extract of the aerial parts of *Paronychia arabica* afforded two oxetane containing lignans, paronychiarabicine A (**1**) and B (**2**), and one new megastigmane, paronychiarabicastigmane A (**3**), alongside a known lignan (**4**), eight known phenolic compounds (**5–12**), one known elemene sesquiterpene (**13**) and one steroid glycoside (**14**). The chemical structures of the isolated compounds were constructed based upon the HRMS, 1D, and 2D-NMR results. The absolute configurations were established *via* NOESY experiments as well as experimental and TDDFT-calculated electronic circular dichroism (ECD). Utilizing molecular docking, the binding scores and modes of compounds **1–3** towards the SARS-CoV-2 main protease (M^{pro}), papain-like protease (PL^{pro}), and RNA-dependent RNA polymerase (RdRp) were revealed. Compound **3** exhibited a promising docking score (−9.8 kcal mol^{-1}) against SARS-CoV-2 M^{pro} by forming seven hydrogen bonds inside the active site with the key amino acids. The reactome pathway enrichment analysis revealed a correlation between the inhibition of *GSK3* and *GSK3B* genes (identified as the main targets of megastigmane treatment) and significant inhibition of SARS-CoV-1 viral replication in infected Vero E6 cells. Our results manifest a novel understanding of genes, proteins and corresponding pathways against SARS-CoV-2 infection and could facilitate the identification and characterization of novel therapeutic targets as treatments of SARS-CoV-2 infection.

Received 29th March 2021
Accepted 15th May 2021

DOI: 10.1039/d1ra02486h

rsc.li/rsc-advances

Introduction

Medicinal plants and their products have been used for the prevention and/or treatment of several diseases.[1–3] According to the World Health Organization (WHO), around 80% of people around the worldwide have used herbal medicinal plants, comprising about 21 000 plant species, as primary health care. According to WHO, around 21 000 plant species have potential for being used as medicinal plants.[4]

The *Paronychia* genus, one of the genera of the family Caryophyllaceae, includes more than 100 plant species all around the world, especially in warm temperature regions such as Africa, the Mediterranean, North and South America and Eurasia.[5] Several traditional uses have been documented for *Paronychia* plants in different areas all over the world such as for the treatment of prostate, bladder, and abdominal ailments, kidney stones, eczema, as a febrifuge and digestive, diabetes, heart pains, as a gastric analgesic and for ulcers, hypoglycemia, as an aperitif and as a diuretic.[6–9]

Extracts and isolated compounds from *Paronychia* plant species have been reported to exhibit significant biological activities such as cytotoxic[10] and antioxidant activities.[9,11,12] Numerous phytochemical constituents from plants belonging to the *Paronychia* genus have been documented, such as gypsogenic acid and polygalacic acid-type saponins, oleanane-type glycosides, flavonoids and tocopherols.[10,11,13–16]

A recent respiratory infectious disease (coronavirus disease (COVID-19)) has been attributed to the novel Severe Acute Respiratory Syndrome coronavirus 2 (SARS-CoV-2).[17] Up to this

[a]*Faculty of Pharmaceutical Sciences, Tokushima Bunri University, Yamashiro-cho, Tokushima, 770-8514, Japan*

[b]*Chemistry of Natural Compounds Department, National Research Centre, Dokki, Giza, 12622, Egypt*

[c]*Chemistry of Medicinal Plants Department, National Research Centre, 33 El-Bohouth St., Dokki, Giza, 12622, Egypt. E-mail: me.fathy@nrc.sci.eg; Fax: +20-233370931; Tel: +20-233371635*

[d]*Computational Chemistry Laboratory, Chemistry Department, Faculty of Science, Minia University, Minia, 61519, Egypt*

[e]*Molecular Genetics and Genome Mapping Laboratory, Genome Mapping Department, Agricultural Genetic Engineering Research Institute (AGERI), Agricultural Research Center (ARC), Giza, 12619, Egypt*

[f]*Department of Pharmaceutical Biology, Institute of Pharmaceutical and Biomedical Sciences, Johannes Gutenberg University, Staudinger Weg 5, 55128 Mainz, Germany*

† Electronic supplementary information (ESI) available. See DOI: 10.1039/d1ra02486h

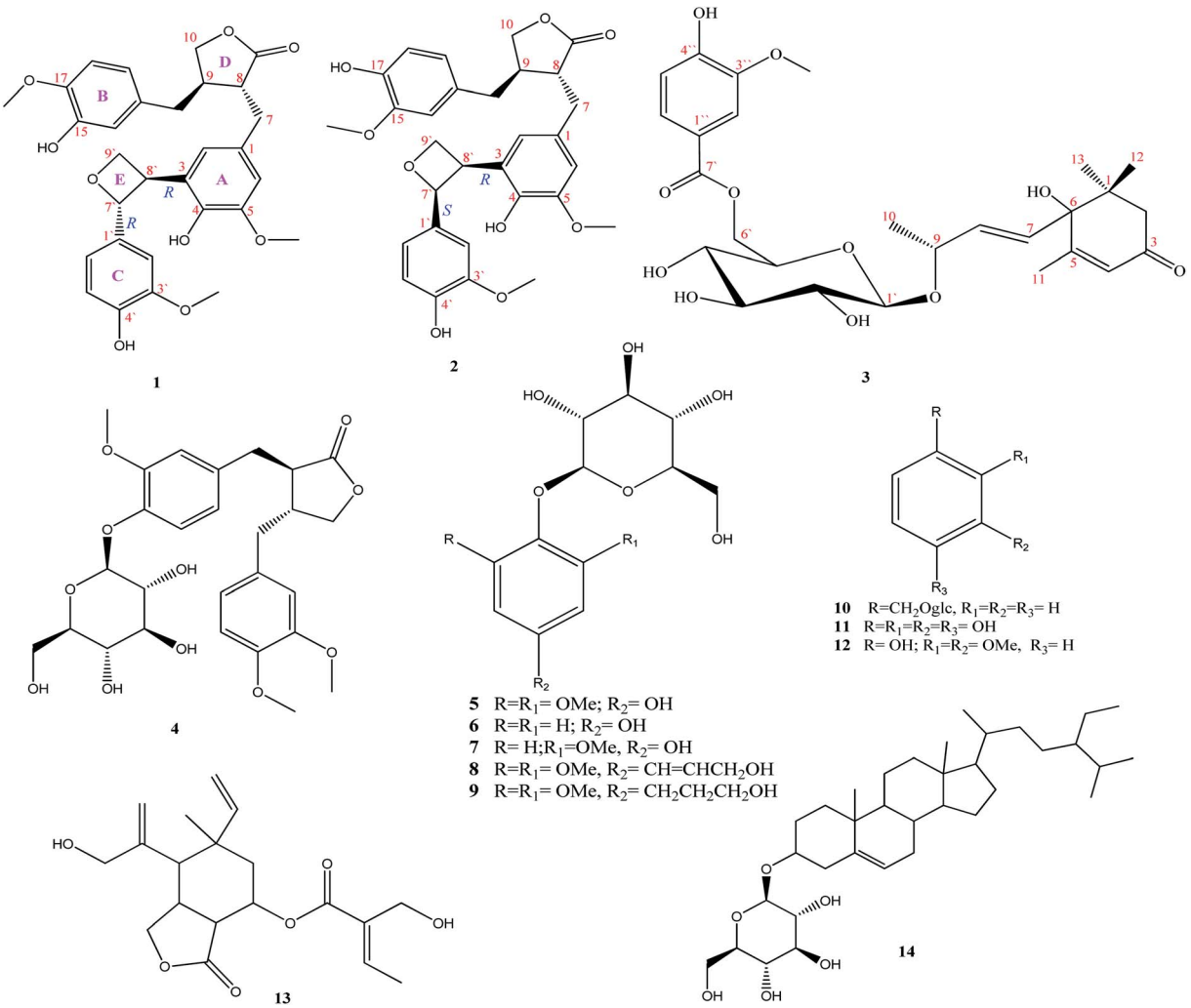

Fig. 1 Structures of the isolated compounds (**1–14**).

date, there are no reports concerning the chemical constituents and/or biological activities of *P. arabica* although the medicinal importance of these plants has been shown. Continuing our work using natural resources for the isolation and identification of bioactive metabolites,[18–23] we described here the isolation and identification of two new oxetane containing lignans **1** and **2**, one new megastigmane **3**, along with a known lignan (**4**), eight known phenolic compounds (**5–12**), a known elemene sesquiterpene (**13**) and one steroid glycoside (**14**) (Fig. 1) from the aerial parts.

Over the past decade, the analysis of pathways and networks has provided a deep understanding of the interactions between genetic variations and therapeutic responses to a large number of drugs in terms of their biological framework.[24] Meanwhile, pathways are known as groups of biological objects connected to specific functions or targets; biological networks are generally assembled in a systems manner, comprising many pathways concurrently.[25] Numerous studies have employed pathway and network-based approaches in targeted therapies to predict drug side effects, explain hazardous toxicity issues and, moreover, to disclose drug resistance mechanisms.[26]

To better understand the effects of targeted therapies in patients, a package of software tools can be used to visualize patient-specific variations and drug targets followed by developing pathways, which are process-oriented representations of biological reactions or biological networks that predict interactions among genes, proteins and other biological entities.[24,27]

To combat COVID-19, prevention of SARS-CoV-2 replication could be achieved by targeting the viral main protease (M^{pro}), papain-like protease (PL^{pro}) and RNA-dependent RNA polymerase (RdRp) enzymes. Therefore, the binding modes and affinities of the isolated compounds were predicted against the three SARS-CoV-2 targets using the molecular docking technique. Furthermore, this study aims to identify targets and pathways enriched in response to megastigmane in terms of SARS-CoV-2 infection.

Results and discussion

The chemical description of the hydro-methanolic extract of *P. arabica* aerial parts provides fourteen metabolites, comprising two new oxetane containing lignans,

paronychiarabicine A (**1**) and B (**2**), a new megastigmane, paronychiarabicastigmane A (**3**) along with eleven known compounds (**4–14**) (Fig. 1).

Paronychiarabicine A (**1**), a white amorphous powder, exhibited a negative optical rotation in methanol [α] −5.1 (C 0.1, MeOH). The molecular formula of **1** was designated as $C_{30}H_{32}O_9$ from the observed TOF-ESI-MS molecular ion peak at 559.1924 $(M + Na)^+$ (calc.: 559.1944; $C_{30}H_{32}O_9Na$) which displayed 15° of unsaturation. The FT-IR spectrum of 1 revealed the characteristic absorption bands of hydroxyl (at 3346 cm^{-1}) and keto (at 1723 cm^{-1}) functional groups. The ^{1}H NMR spectrum of **1** (Table 1) showed eight aromatic protons at δ_H 6.42 dd (1H, J = 8.2, 2.0 Hz), 6.46 brs (1H), 6.58 d (1H, J = 1.3 Hz), 6.50 d (1H, J = 1.9 Hz), 6.65 dd (2H, J = 8.2, 2.0 Hz), 6.72 dd (1H, J = 8.2, 2.0 Hz), and 6.82 d (1H, J = 1.9 Hz). Two oxygenated aliphatic methylenes at δ_H 3.71 ddd (J = 7.5, 3.8, 2.0 Hz), 3.61 ddd (J = 7.5, 3.8, 2.0 Hz) and at δ_H 3.83 dd (J = 7.3, 1.6 Hz), 4.09 dd (J = 7.3, 1.6 Hz)] as well as one oxygenated methine at δ_H 5.41 d (J = 6.9 Hz) were assigned. Additionally, three methoxy groups at δ_H 3.64 (s, 6H) and 3.72 s were characterized. The ^{13}C NMR of **1** (Table 1) displayed thirty carbon resonances that were categorized, depending upon HSQC and DEPT-135, into 11 quaternary, 12 methines, 4 methylenes, and 3 methyls. The quaternary carbons were characterized into a keto group at δ_C 180.2, six oxygenated aromatic carbons at δ_C 144.0, 144.9, 146.1, 146.9 and 147.7 (2 × C), and four substituted aromatic carbons at δ_C 128.6, 130.1, 131.3 and 133.4. The methines were also assigned to eight aromatic carbons at δ_C 108.9, 112.0, 113.5, 114.7, 114.8, 117.7, 118.3 and 120.9, one oxygenated carbon at δ_C 87.7, and three aliphatic ones at δ_C 41.3, 46.5 and 54.0. By the same method, four methylenes were identified at δ_C 34.2 and 37.5 and two oxygenated at δ_C 63.6 and 71.5. The three methyls present at δ_C 54.9 (2 × C) and 55.3 were characterised as for three methoxy groups.

The analysis of the 1D NMR of **1** (Table 1) as well as the 2D NMR (Fig. 2) displayed three aromatic rings: (i) a tetra-substituted ring (ring A), (ii) a tri-substituted ring (ring B) and (iii) a tri-substituted ring (ring C). The HMBC correlations of H-1

Table 1 ^{1}H and ^{13}C NMR data of **1** and **2** (CD3OD, 500 MHz)[a]

	Paronychiarabicine A (**1**)			Paronychiarabicine B (**2**)		
No.	δ_H, mult. (J Hz)	δ_C		δ_H mult. (J Hz)	δ_H	
1	—	131.3	s	—	132.0	s
2	6.46 br s	117.7	d	6.48 br s	116.9	d
3	—	128.6	s	—	128.8	s
4	—	146.9	s	—	146.7	s
5	—	147.7	s	—	147.7	s
6	6.58 d (1.3)	113.5	d	6.65 d (2.0)	112.9	d
7a	2.83 dd (14.0, 5.5)	34.2	t	2.76 dd (14.1, 5.4)	34.0	t
7b	2.74 dd (14.0, 5.5)			2.59 dd (14.1, 5.4)		
8	2.59 m	46.5	d	2.58 m	46.4	d
9	—	180.2	s	—	180.3	s
10a	3.83 dd (7.3, 1.6)	71.5	t	3.84 t (16.9)	71.5	t
10b	4.09 dd (7.3, 1.6)			4.11 dd (7.6, 1.4)		
11	2.42 m	41.3	d	2.43 m	41.1	d
12	2.41 m	37.5	t	2.49 d (1.6), 2.42 d (1.6)	37.7	t
13	—	130.1	s	—	129.9	s
14	6.50 d (1.9)	112.0	d	6.46 d (1.9)	112.6	d
15	—	144.0	s	—	145.0	s
16	—	144.9	s	—	144.0	s
17	6.65 dd (8.2, 2.0)	114.7	d	6.66 dd (8.1, 1.9)	114.7	d
18	6.42 dd (8.0, 2.0)	120.9	d	6.58 d (8.0)	121.7	d
1′	—	133.4	s	—	133.2	s
2′	6.82 d (1.9)	108.9	d	6.85 d (2.0)	109.1	d
3′	—	147.7	s	—	147.6	s
4′	—	146.1	s	—	146.2	s
5′	6.65 dd (8.2, 2.0)	114.8	d	6.66 dd (8.1, 1.9)	114.7	d
6′	6.72 dd (8.2, 2.0)	118.3	d	6.73 dd (8.3, 1.9)	118.3	d
7′	5.41 d (6.9)	87.7	d	5.39 d (6.4)	87.7	d
8′	3.34 dd (7.5, 11.4)	54.0	d	3.35 m	53.9	d
9′a	3.71 ddd (7.5, 3.8, 2.0)	63.6	t	3.69 ddd (8.0, 3.9, 2.6)	63.4	t
9′b	3.61 ddd (7.5, 3.8, 2.0)			3.64 ddd (7.0, 4.3, 1.3)		
5-OMe	3.64 s	54.9	q	3.67 s	55.0	q
15-OMe	—	—		3.71 s	55.3	q
16-OMe	3.72 s	55.3	q	—	—	
3′-OMe	3.64 s	54.9	q	3.70 s	55.0	q

[a] s: quaternary, d: methine, t: methylene, q: methyl.

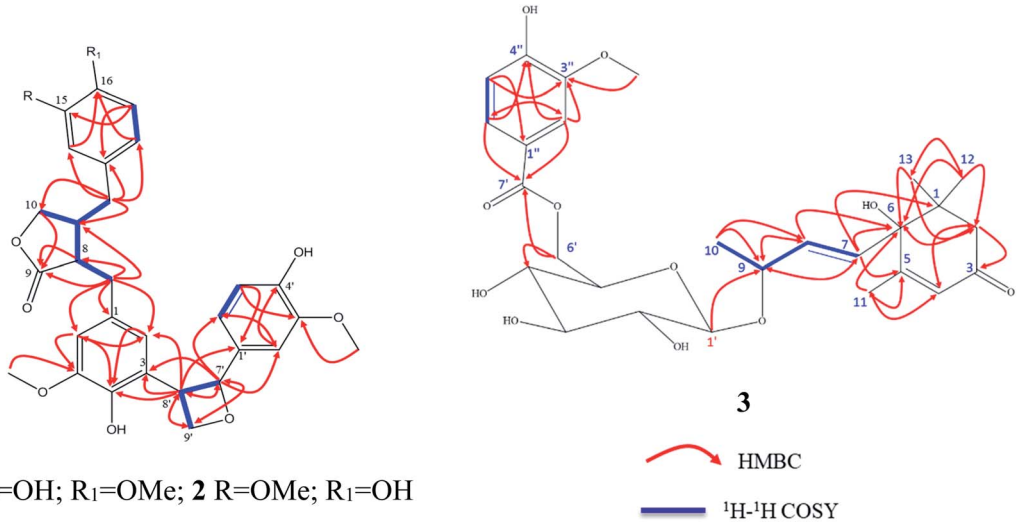

Fig. 2 $^{1}H-^{1}H$ COSY and HMBC of **1–3**.

at δ_H 6.46 br s/C-6 (δ_C 113.5; J^3), H-6 at δ_H 6.46 br s/C-3 (δ_C 146.9; J^3) and H-6/C-5 (δ_C 147.7; J^2) as well as H-2/C-3 (δ_C 128.6; quaternary carbon; J^2) and H-2/C-1 (δ_C 131.3; quaternary carbon; J^2) established the tetra-substituted ring (ring A). Additionally, the observed strong J^3-HMBC correlation of the methyl proton at δ_H 3.64 s and the oxygenated carbon C-5 at δ_C 147.7 confirmed that C-5 was methoxylated. Also, the tri-substituted ring (ring B) was constructed depending upon the HMBC correlations of H-14 at 6.50 d (J = 1.9 Hz)/C-16 (δ_C 144.9; J^3), H-14/C-18 (δ_C 120.9; J^3), H-18 at δ_H 6.42 dd (J = 8.2, 2.0 Hz)/C-16, (H-18 δ_C 120.9) and H-17 at δ_H 6.65 dd (2H, J = 8.2, 2.0 Hz)/C-15 (δ_C 144.0; J^3) alongside H-17/C-13 (δ_C 130.1; quaternary carbon; J^3). The methoxylation of C-16 was deduced by the strong J^3-HMBC correlation of the methyl proton at δ_H 3.72 s/C-16.

The $^{1}H-^{1}H$ COSY correlations of H-8 at δ_H 2.59 m/H-11 at δ_H 2.42 m, H-11/H-10 at δ_H [3.83 dd (J = 7.3, 1.6 Hz); 4.09 dd (J = 7.3, 1.6 Hz); oxygenated methylene] along with the strong HMBC correlations of H-8/C-9 (1δ_C 80.2; carbonyl carbon, J^2) and H-10/C-9 (J^3) were used to deduce the disubstituted dihydrofuranone ring (ring D). Also, the $^{1}H-^{1}H$ COSY correlations of H-7′ at δ_H 5.41 d (J = 6.9 Hz)/H-8′ at δ_H 3.34 t (J = 16.8 Hz) and H–H-8′/H-9′ at δ_H [3.71 ddd (J = 7.5, 3.8, 2.0, Hz); 3.61 ddd (7.5, 3.8, 2.0)], supported with the HMBC correlations of H-7′/C-8′ (δ_C 54.0; J^2), H-9′/C-7′ (oxygenated methane; δ_C 87.7; J^3) and H-8′/C-9′ (oxygenated methylene; δ_C 63.6; J^2) confirmed the presence of the oxetane ring as ring E.

The $^{1}H-^{1}H$ COSY correlations of H-11/H-12 at δ_H 2.41 m (aliphatic methylene) as well as the HMBC correlation of H-12/C-11 (δ_C 41.3; J^2), H-12/C-10 (δ_C 71.5; J^3), H-12/C-13 (δ_C 130.1; J^2), H-12/C-14 (δ_C 112.0; J^3) and H-12/C-18 (δ_C 120.9; J^3) construct the linkage of aromatic ring B and the disubstituted dihydrofuranone ring (ring D) *via* the methylene carbon C-12.

The 2D NMR spectrum of **1** exhibited clear HMBC correlations of H-7′ (δ_H 5.41 d, J = 6.9 Hz)/C-1′ (δ_C 133.4; J^2), H-8′ (δ_H 3.34 m)/C-1′ (J^3), H-7′/C-2′ (δ_C 108.9; J^3) and H-7′/C-6′ (δ_C 118.3; J^3). At the same time, HMBC correlations of H-7′/C-3 (δ_C 128.6; J^3), H-8′/C-3 (J^2), H-8′/C-2 (δ_C 117.7; J^3) and H-8′/C-4 (δ_C 146.9; J^3) were assigned. These HMBC correlations construct the 3→8′ attachment of ring A by the oxetane moiety (ring E) as well as the 1′→7′ of ring C by the oxetane moiety (ring E).

The absolute configuration of **1** was confirmed from the J coupling constants as well as the NOESY experiments (Fig. 3). Numerous reports have described how the low J coupling constants between both H-7′ and H-8′ (6.9–7.6 Hz) can be used to deduce the *trans* orientation of diphenyloxetanes.[28–30] In **1**, the ^{1}H NMR exhibited low coupling constant values of 7.1 Hz, confirming the *trans* orientation of H-7′ and H-8′. The ^{13}C NMR chemical shifts of C-7′ and C-8′ at δ_C 87.7 and 54.0, respectively, were totally in agreement with a previously published new oxetane containing neolignan that deduced the same configurations.[30,31] Also, the NOESY correlations of H-9′b [δ_H 3.61 ddd (J = 7.5, 3.8, 2.0 Hz)]/H-7′, H-9′a [δ_H 3.71 ddd (J = 7.5, 3.8, 2.0 Hz)]/H-8′ and H-8′/H-2 [δ_H 6.46 br s] confirmed the *trans* orientation of H-7′ and H-8′. Additionally, NOESY correlations of H-2/H-7 [δ_H 2.83 dd (J = 14.0, 5.5 Hz)], H-7/H-8 [δ_H 2.59 m], H-8/H-10 [δ_H 3.83 dd (J = 7.3, 1.6 Hz)], H-7/H-11 [δ_H 2.42 m] and H-11/H-12 [δ_H 2.41 m] were assigned.

To elucidate the absolute configuration of **1**, a Boltzmann-weighted TDDFT-ECD spectrum was generated and compared to the experimental one (Fig. 4). The TDDFT-simulated ECD spectrum of 7′*R*,8′*R* was in a good agreement with the corresponding experimental ECD spectrum of **1** (Fig. 4). From all of the above-described spectroscopic data, **1** was shown to be a novel oxetane containing lignan, paronychiarabicine A.

Paronychiarabicine B (**2**), a yellow amorphous powder, showed a negative optical rotation in methanol [α] + 6.6 (C 0.1, MeOH). The molecular formula of **2** was established as $C_{30}H_{32}O_9$ from the observed HR-CIMS molecular ion peak at 536.2030 $(M)^+$ (calc.: 536.2046; $C_{30}H_{32}O_9$), which revealed 15° of unsaturation. The FT-IR spectrum of **2** revealed the characteristic absorption bands of hydroxyl (at 3346 cm^{-1}) and keto (at 1723 cm^{-1}) functional groups. Carefully analysis of the ^{1}H and ^{13}C NMR of **2** (Table 1) allowed us to deduce that this compound has same skeleton of **1** except for (i) the down field shift of C-15

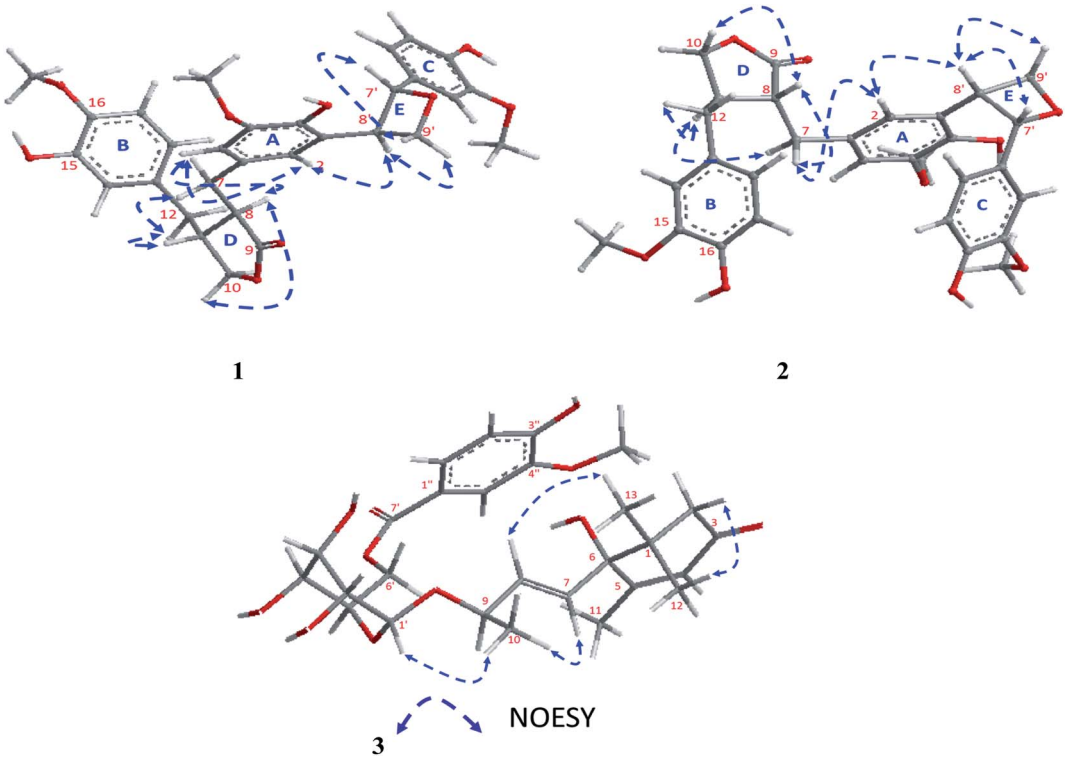

Fig. 3 Key NOESY results of **1**–**3**.

by 1 ppm at δ_C 145, (ii) the up field shift of C-16 by 0.9 ppm at δ_C 144.0, and (iii) the clear down field shift of H-18 by 0.16 ppm at δ_H 6.58 d (J = 8.0 Hz) as well as C-18 by 0.6 ppm at δ_C 121.7. Through the careful analysis of the 2D NMR, the methoxy and hydroxy groups were localized at C-15 and C-16, instead of the opposite in **1**, *via* the HMBC correlations of H-18/C-16 (J^3), H-17 [δ_H 6.66 dd (2H, J = 8.1, 1.9 Hz)]/C-15 (J^3) and OMe (δ_H 3.71 s)/C-15 (J^3) (Fig. 2).

The stereochemistry of **2** was established using the coupling constants and NOESY correlations. Regarding to the reports of Saphier *et al.*, 2005, the *cis* and *trans* isomers of diphenyloxetanes have different R_f values over a plate of silica gel eluted using *n*-hexane–EtOAc in which the *cis* isomer has a lower R_f than that of the *trans* isomer.[29] Also, Saphier *et al.*, 2005, the *cis* reported that the appearance of H-7′ with a lower coupling constant (<6.9 Hz), as well as the NOE effect of H-8′ due to proximity, allowed the β orientation of H-7′ and H-8′ to be deduced.[29] For **2**, the R_f (0.62) was found to be lower than that of **1** (0.67) and the coupling constant of H-7′ was assigned at 6.4 Hz (<6.9 Hz), which is in full agreement with the above mentioned

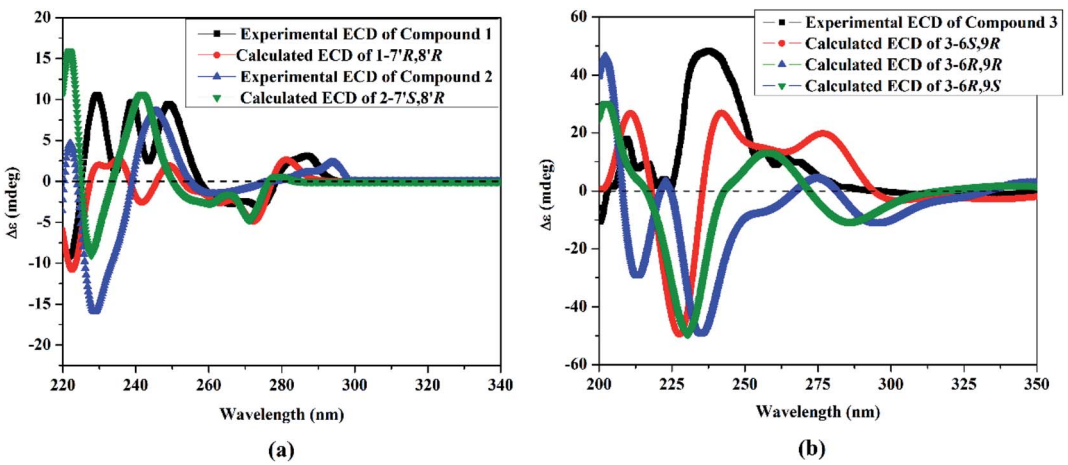

Fig. 4 (a) Experimental electronic circular dichroism (ECD) in methanol of **1** (in black) and **2** (in blue), compared with the TDDFT-simulated ECD spectra of **1**-7′*R*,8′*R* (in red) and **2**-7′*S*,8′*R* (in green). (b) Experimental ECD in methanol of compound **3** (in black), compared with the TDDFT-simulated ECD spectra of **3**-6*S*,9*R*, **3**-6*R*,9*R* and **3**-6*R*,9*S*.

reports.[28,29] The NOESY correlations of **2** exhibited the same correlations of **1** except for some different correlations that deduced the β orientation of H-7′ and H-8′, such as (i) the absence of correlation of H-9′b [δ_H 3.64 ddd (J = 7.0, 4.3, 1.3 Hz)]/H-7′ [5.39 d (J = 6.4 Hz)], (ii) the presence of the correlations of H-9′a [δ_H 3.69 ddd (J = 8.0, 3.9, 2.6 Hz)]/H-8′ (δ_H 3.35 m), and H-8′/H-2 [δ_H 6.48 br s] and (iii) the assignment of the correlation of H-8′/H-7′ (Fig. 3). Using the same method, the absolute configuration of **2** was confirmed based upon comparing the Boltzmann-weighted TDDFT-ECD spectra with the experimental one (Fig. 4). The TDDFT-simulated ECD spectrum of the 7′*S*,8′*R* isomer was in good agreement with the experimental ECD of **2** (Fig. 4). From all of the mentioned data, **2** was established as a novel oxetane containing lignin, namely paronychiarabicine B.

Paronychiarabicastigmane A (**3**), a white amorphous powder, exhibited a negative optical orientation ([α] −6.6 (C 0.1, MeOH)). The molecular formula of **3** was determined as $C_{27}H_{36}O_{11}$ from the two positive mode LR-FAB-MS molecular ion peaks at the *m*/*z* 537 $(M + 1)^+$ and 559 $(M + Na)^+$, deduced from the HR-FAB-MS at *m*/*z* 559.2157 $(M + 1)^+$, (calc.: 559.2155; $C_{27}H_{36}O_{11}Na$), and it exhibited 10 degrees of unsaturation. The FT-IR exhibited characteristic absorption bands of hydroxyl and keto groups at 3343 cm^{-1} and 1725 cm^{-1}, respectively. The ^1H NMR of **3** (Table 2) revealed three protons of the 1,3,4-trisubtituted aromatic ring [at δ_H 6.84 d (J = 8.1 Hz), 7.55 d (J = 8.3 Hz) and 7.58 br s], one anomeric proton of the hexoside moiety [at δ_H 4.36 d (J = 7.8 Hz)] as well as the hexoside protons [at δ_H 3.18 m, 3.25 m, 3.28 m, 3.35 m, 3.67 m and 3.87 d (J = 1.8 Hz)], three aliphatic olefinic methine protons [at δ_H 5.87 d (2H, J = 6.6 Hz) and 5.88 d (J = 2.0 Hz)], one aliphatic methylene proton [at δ_H 2.16 d (J = 16.8 Hz) and 2.53 d (J = 20.0 Hz)], four methyl protons [at δ_H 1.05 (s, 6H), 1.31 d (J = 6.4 Hz) and 1.93 d (J = 1.2 Hz)] and one methyl of the methoxy group at δ_H 3.91 s.

Table 2 ^1H and ^{13}C NMR data of **3** (CD_3OD, 500 MHz)[a]

No.	Paronychiarabicastigmane A (**1**)							
	δ_H, mult. (J Hz)	δ_C			δ_H, mult. (J Hz)	δ_C		
1	—	41.0	s	1″	—	122.7	s	
2a	2.16 d (16.8)	49.3	t	2″	7.58 br s	112.4	d	
2b	2.53 d (20.0)			3″	—	147.2	s	
3	—	199.8	s	4″	—	150.9	s	
4	5.88 d (2.0)	125.8	d	5″	6.84 d (8.1)	114.3	d	
5	—	165.9	s	6″	7.55 d (8.3)	123.8	d	
6	—	78.6	s	3″-OMe	3.91 s	55.0	q	
7	5.87 d (6.6)	130.1	d					
8	5.87 d (6.6)	133.9	d					
9	4.43 m	75.9	d					
10	1.31 d (6.4)	19.8	q					
11	1.93 d (1.2)	18.2	q					
12	1.05 s	22.0	q					
13	1.05 s	22.3	q					
1′	4.36 d (7.8)	101.3	d					
2′	3.18 m	73.8	d					
3′	3.25 m	76.6	d					
4′	3.28 m	70.2	d					
5′	3.35 m	76.7	d					
6′	3.67 m							
3.87 d (1.8)	61.4	t					
7′	—	167.0	s					

[a] s: quaternary, d: methine, t: methylene, q: methyl.

Twenty-seven carbon resonances were characterized in the ^{13}C NMR of **3** (Table 2). The complete examination of the ^{13}C-NMR and ^1H-NMR revealed the β-glucopyranoside moiety by the six typical substantiated carbons. With more details, these carbons were classified, depending upon the DEPT-135 and HSQC experiments, into 8 quaternary carbons [an α,β-unsaturated keto carbon (at δ_C 199.8) and an ester keto carbon (at δ_C 167.0), three substituted aromatic carbons (at δ_C 122.7, 147.2, 150.9), one aliphatic olefinic carbon (at δ_C 165.9), one oxygenated carbon (at δ_C 78.6) and one aliphatic (at δ_C 41.0)], one anomeric carbon (at δ_C 101.3) as well as 5 methines of the sugar moiety (at δ_C 61.4, 70.2, 73.8, 76.6, 76.7), three aliphatic olefinic carbons (at δ_C 125.8, 130.1, 133.9), three aromatic methines (at δ_C 112.4, 114.3, 123.8), one oxygenated methine (at δ_C 75.9), one aliphatic methylene (at δ_C 49.3), four methyls (at δ_C 18.2, 19.8, 22.0, 22.3) and one methyl of the methoxy group (at δ_C 55.0)].

From the careful assignment of the 1D NMR, the structure of **3** was established as a megastigmane skeleton.[33] This structure was deduced *via* 2D NMR using ^1H ^1H COSY and HMBC (Fig. 2). In HMBC, the correlations of H_3-12 [δ_H 1.05 s]/C_{H3}-13 [δ_C 22.3, J^3], H_3-13 [δ_H 1.05 s]/C_{H3}-12 [δ_C 22.0, J^3], H_3-12/C_{H2}-2 [δ_C 49.3, J^3], H_3-12/C-6 [δ_C 78.6, J^3], H_2-2 [δ_H 2.16 d (J = 16.8 Hz)] and 2.53 d (J = 20.0 Hz)]/C-6 [J^3], H_2-2/C-3 [δ_C 199.8, J^2], H_2-2/C-4 [δ_C 125.8, J^2], H_3-11 [δ_H 1.93 d (J = 1.2 Hz)]/C-5 [δ_C 165.9, J^2], H_3-11/C-4 [J^3] and H_3-11/C-6 [J^3] were used to deduce the megastigmane skeleton. Consequently, the ^1H ^1H COSY correlations of H-7 [δ_H 5.87 d (J = 6.6 Hz)]/H-8 [δ_H 5.87 d (J = 6.6 Hz)], H-8/H-9 [δ_H 4.43 m], H-9/H_3-10 [δ_H 1.31 d (J = 6.4 Hz)] and the HMBC correlations of H-7/C-6 [δ_C 78.6, J^2], H-7/C-1 [δ_C 41.0, J^3], H-7/C-1 [δ_C 41.0, J^3], H-7/C-5 [J^3], H_3-10/C-8 [δ_C 75.9, J^2], H_3-10/C-8 [δ_C 133.9, J^3] and H-1′ [(δ_H 4.36 d (J = 7.8 Hz)]/C-9 [δ_C 75.9, J^3] as well were used to elucidate that megastigmane attached to the glucose moiety *via* C-9. The ^1H ^1H COSY correlations of H-5″ [δ_H 6.84 d (J = 8.1 Hz)]/H-6″ [δ_H 7.55 d (J = 8.3 Hz)] together with the HMBC correlations of H-5″/C-4″ [δ_C 150.9, J^2], H-5″/C-3″ [δ_C 147.2, J^3], H-2″ [δ_H 6.84 d (J = 8.1 Hz)]/C-3″ [J^2], H-2″/C-4″ [J^3], OMe [δ_H 3.91 s]/C-3″ [δ_C 147.2, J^3], H-2″/C-1″ [δ_C 122.7, J^2], H-2″/C-6″ [δ_C 123.8, J^3], H-6″/C-1″ [J^3], H-2″/C-7″ [δ_C 122.7, ester keto, J^3] and H-6″/C-7″ [J^3] assigned the phenolic moiety as a 3″-methoxy-4″-hydroxy-benzen-1″-carboxylic acid ester. Continuing, the up field shift of the sugar carbon, C-6′ at δ_C 61.4 as well as the HMBC correlations of H-6′/C-7′ [δ_C 167.0, J^3], H-6″/C-7′ [J^3] and H-2″/C-7′ [J^3] were used to deduce that the attachment of the sugar with the phenolic moiety was *via* the ester linkage between the sugar carbon H-6′ and the carboxylic acid carbon C-7′. The sugar moiety was determined to be D-glucose by total acid hydrolysis and examinations by TLC with different standard hexosides. The β orientation of the anomeric proton H-1′ was firstly determined by the value of the coupling constant (d, J = 7.8 Hz).[32,33]

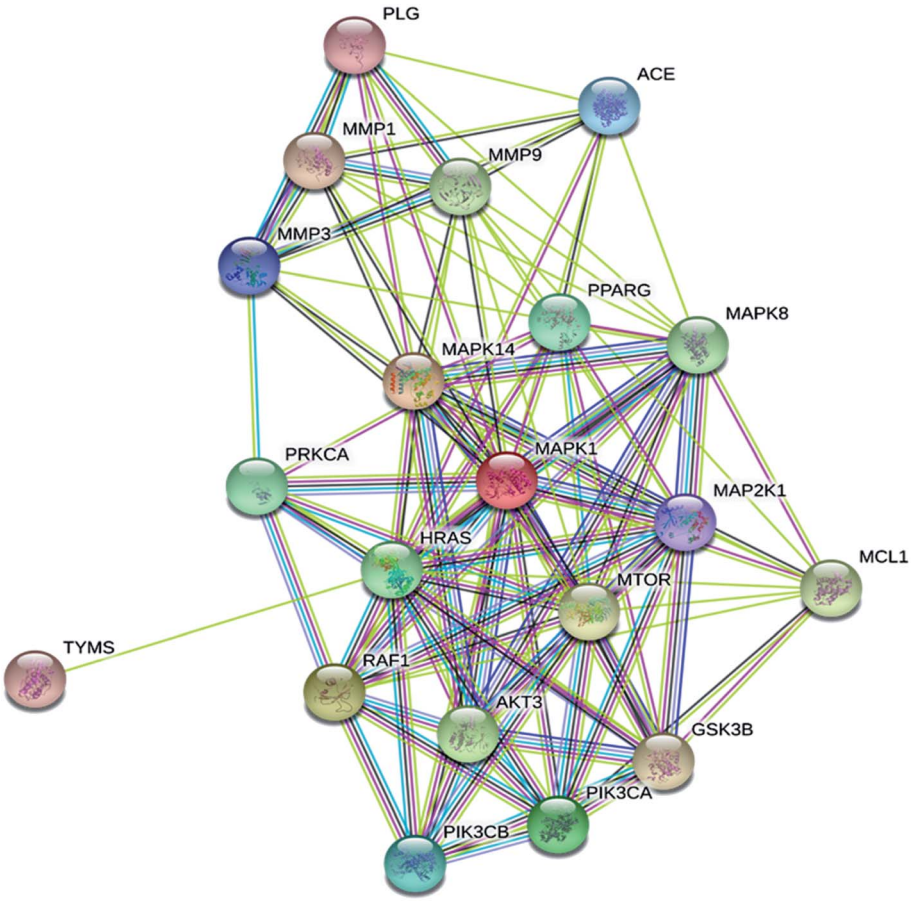

Fig. 5 STRING protein–protein interaction (PPI) network for the top 20 targets for megastigmane (**3**) as a potent SARS inhibitor.

From the NOESY experiment, H-1′-β exhibited a strong correlation with Me-10 [δ_H 1.31 d ($J = 6.4$ Hz) which allowed the α orientation of H-9 to be deduced. Additionally, NOESY correlations between H-8 [δ_H 5.87 d ($J = 6.6$ Hz)]/Me-13 [δ_H 1.05 s] and H-2b [δ_H 2.53 d ($J = 20.0$ Hz)]/Me-12 [δ_H 1.05 s] were detected. The *R*-orientation of C-9 was determined based upon

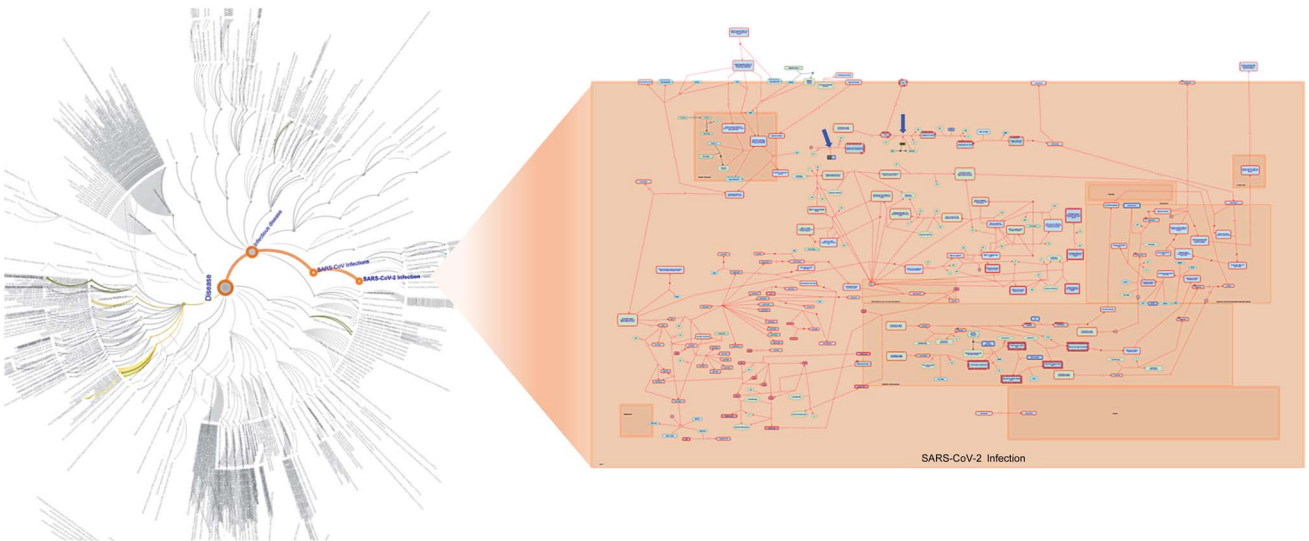

Fig. 6 (A) The reactome map illustration of disease pathways influenced by the top 20 gene targets responding to megastigmane (**3**) in terms of SARS-CoV-2 infection. The colours denote over-representation of that pathway in the input dataset. Light grey signifies pathways which are not significantly over-represented.

Table 3 Top ten pathways of megastigmane (3) targets resulting from pathway enrichment analysis (PEA)

Pathway	Pathway size	Number of targets in the pathway	*P*-value	FDR	Targets in pathway (hit genes)
Cytokine signaling in the immune system	780	12	7.19×10^{-9}	6.87×10^{-7}	*MAP2K1*, *MMP1*, *MMP3*, *PIK3CB*, *MAPK14*, *MMP9*, *MAPK8*, *PIK3CA*, *MAPK1*, *RAF1*, *HRAS*, *MCL1*
Signaling by receptor tyrosine kinases	421	10	4.22×10^{-9}	6.87×10^{-7}	*MAP2K1*, *PLG*, *PRKCA*, *PIK3CB*, *MAPK14*, *MMP9*, *MTOR*, *PIK3CA*, *MAPK1*, *HRAS*
Signaling by interleukins	435	10	5.78×10^{-9}	6.87×10^{-7}	*MAP2K1*, *MMP1*, *MMP3*, *PIK3CB*, *MAPK14*, *MMP9*, *MAPK8*, *PIK3CA*, *MAPK1*, *MCL1*
Axon guidance	492	10	1.87×10^{-8}	1.20×10^{-6}	*GSK3B*, *MAP2K1*, *PRKCA*, *PIK3CB*, *MAPK14*, *MMP9*, *MAPK8*, *PIK3CA*, *MAPK1*, *HRAS*
Signaling by NTRK1 (TRKA)	73	6	8.48×10^{-9}	6.87×10^{-7}	*MAP2K1*, *PIK3CB*, *MAPK14*, *PIK3CA*, *MAPK1*, *HRAS*
VEGFA–VEGFR2 pathway	86	6	2.23×10^{-8}	1.20×10^{-6}	*PRKCA*, *PIK3CB*, *MAPK14*, *MTOR*, *PIK3CA*, *HRAS*
Signaling by NTRKs	92	6	3.31×10^{-8}	1.50×10^{-6}	*MAP2K1*, *PIK3CB*, *MAPK14*, *PIK3CA*, *MAPK1*, *HRAS*
Signaling by VEGF	94	6	3.76×10^{-8}	1.50×10^{-6}	*PRKCA*, *PIK3CB*, *MAPK14*, *MTOR*, *PIK3CA*, *HRAS*
MAP2K and *MAPK* activation	18	4	6.85×10^{-8}	2.19×10^{-6}	*MAP2K1*, *MAPK1*, *RAF1*, *HRAS*
Gastrin–CREB signalling pathway *via PKC* and *MAPK*	18	4	6.85×10^{-8}	2.19×10^{-6}	*MMP3*, *PRKCA*, *MAPK1*, *HRAS*

the ^{13}C NMR chemical shift at δ_C 75.9 (Matsuda *et al.*, 1996 [34] and Wang *et al.*, 2011 [35]). To confirm the absolute configuration of **3**, the TDDFT-simulated ECD spectra for **3**-6*S*,9*R*, **3**-6*R*,9*R* and **3**-6*R*,9*S* were generated and compared to the experimental spectrum (Fig. 4). The observed positive Cotton effect at 238 nm in the ECD of **3** demonstrated the *S*-configuration of C-6 [34] as well as the TDDFT-calculated ECD of 3-6*S*,9*R* being in a good agreement with the experimental spectrum (Fig. 4). From all of these data, **3** was identified as Paronychiarabicastigmane A.

In addition to compounds **1–3**, eleven metabolites were isolated and identified as matairesinol 4′-*O*-glucoside (**4**),[36] leonuriside A (**5**),[37] arbutine (**6**),[38] isotachioside (**7**),[39] syringin (**8**),[40] dihydrosyringin (**9**),[41] benzyl-*O*-β-D-glucopyranoside (**10**),[42] benzene-1,2,3,4-tetraol (**11**),[43] 2,3-dimethoxyphenol (**12**),[44] 8α-

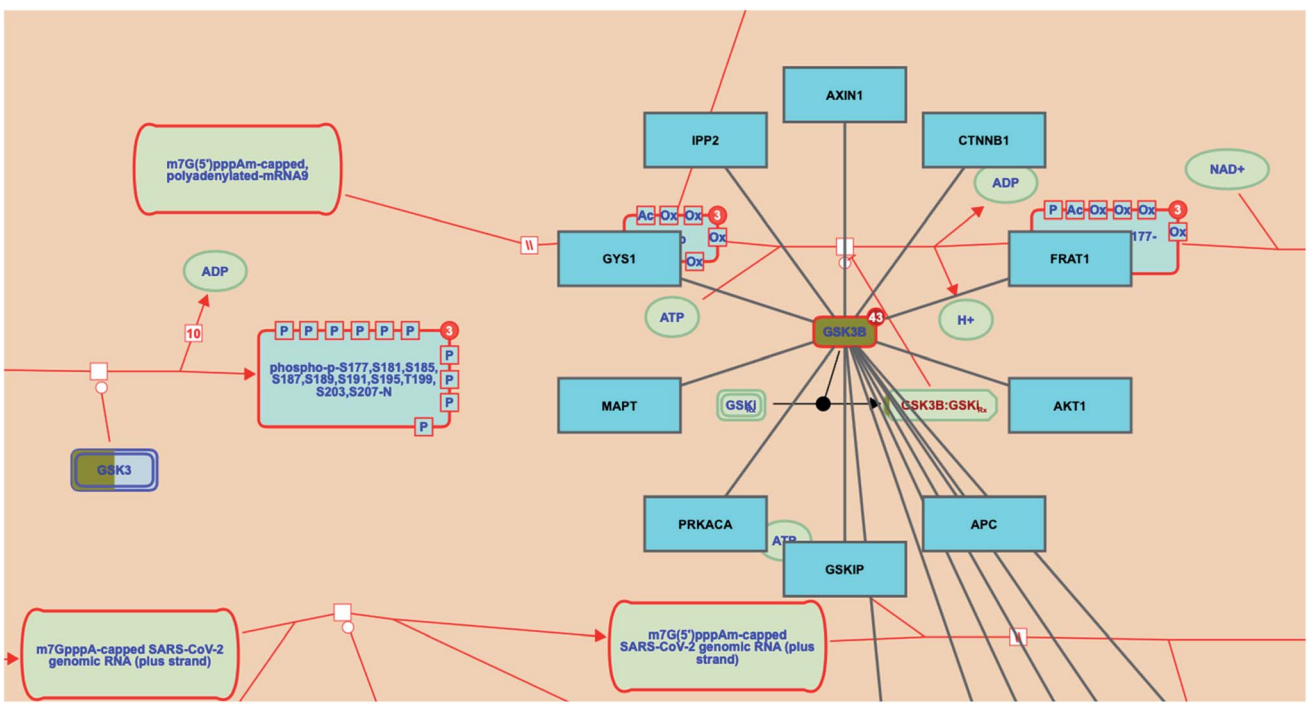

Fig. 7 SARS-CoV-2 infection pathway showing the targets (*GSK3B*; highlighted in dark yellow) in response to megastigmane (**3**) as a potent SARS-CoV-2 inhibitor. The interactor genes were highlighted in blue.

(2′-hydroxymethyl-2′-butenoyloxy) derivative of dehydromelitensin (**13**)[45] and daucosterin (**14**).[46]

Megastigmane (**3**) protein targets associated with SARS diseases were predicted using the SwissTargetPrediction-DisGeNET online tools. One hundred and seventeen genes were identified with genes classified using Venn diagram comparison. Based on the PPI network profiles, a STRING web-tool and Cytoscape 3.8.0 for visualization were used to explore the predicted gene targets of megastigmane (**3**) (Fig. 5). The top 20 genes responding to megastigmane (**3**) included *HRAS*, *MAPK1*, *MMP9* and MTOR.

For further investigation of the megastigmane target–function interactions, pathway enrichment analysis and Boolean Network modeling were carried out. The reactome hierarchy map of megastigmane (**3**) identified disease pathways which were influenced by the top 20 gene targets responding to megastigmane (**3**) in terms of SARS-CoV-2 infection (Fig. 6). Out of the top ten biological pathways resulting from the reactome pathway enrichment analysis, four major biological pathways for megastigmane (**3**) of cytokine signaling in the immune system, signaling by receptor tyrosine kinases, signaling by interleukins and axon guidance with a high significance (FDR <0.00001%) were identified (Table 3).

Investigating the reactome pathway enrichment analysis results highlighted a set of two genes (*GSK3* and *GSK3B*) that represent significant biological targets in the action of megastigmane (**3**) as a potent SARS-CoV-2 inhibitor. Additionally, the reactome pathway enrichment analysis for SARS-CoV-2 revealed that *GSK3B* gene interacts with other genes/interactors including *AXIN1*, *CTNNB1*, *FRAT1*, *AKT1*, *APC*, *GSKIP*, *PRKACA*, *MAPT*, *GYS1* and *IPP2* (Fig. 7).

The SARS-CoV-2 infection pathway

Many additional host factors are involved in the SARS-CoV-2 genome transcription/replication. For instance, the coronavirus N protein plays an important role as a RNA chaperone which enables template switching.[47] Importantly, the N protein of SARS-CoV-1 is phosphorylated by the host glycogen

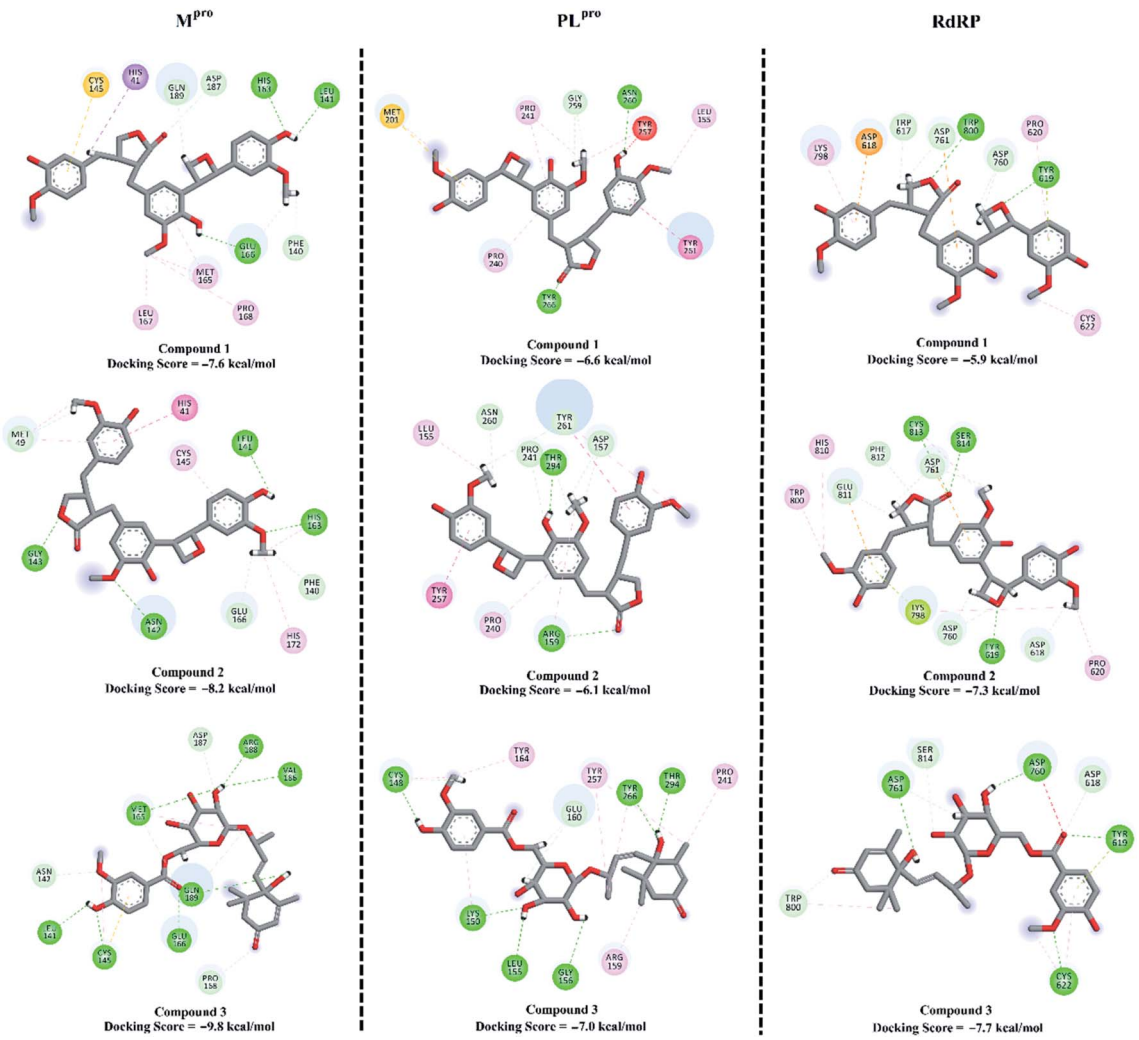

Fig. 8 Predicted docking score and binding mode of compounds **1–3** inside the active site of SARS-CoV-2 main protease (M^{pro}), papain-like protease (PL^{pro}) and RNA-dependent RNA polymerase (RdRp). Interactions: conventional hydrogen bond (green), carbon–hydrogen bond (pale green), pi–sigma and pi–pi (violet), pi–sulfur (yellow), alkyl and pi–alkyl (pale violet), unfavorable donor–donor (red), pi–lone-pair (lemon yellow).

synthase kinase 3 (*GSK3*), and its inhibition was found to significantly inhibit viral replication.[48]

Prospective SARS-CoV-2 inhibitors

To combat COVID-19, the potentials of the isolated compounds **1–3** as SARS-CoV-2 M^{pro}, $PL^{pro}$and RdRp inhibitors were predicted. The investigated compounds were docked into the active sites of the SARS-CoV-2 targets using AutoDock4.2.6 software.[49] The predicted docking scores and the 2D representations of the binding modes of compounds **1–3** inside the active site of SARS-CoV-2 targets are depicted in Fig. 8.

According to the molecular docking calculations, compounds **1–3** demonstrated better binding affinities towards SARS-CoV-2 M^{pro} compared to those with PL^{pro} and RdRp. Comparing the molecular docking results towards M^{pro} revealed that compound **3** exhibited an outstanding binding affinity towards M^{pro} with a docking score of −9.8 kcal mol^{-1}, forming seven hydrogen bonds with the key amino acids inside the active site (Fig. 8). Compounds **1** and **2** showed moderate binding affinities with docking scores of −7.6 and −8.2 kcal mol^{-1} with M^{pro}, forming three and four hydrogen bonds, respectively.

Experimental section

General experimental procedures

Optical rotations were measured on a JASCO P-2300 polarimeter (Tokyo, Japan).^{1}H (500 MHz), and ^{13}C NMR (125 MHz) spectra were recorded on a Bruker 500 NMR spectrometer (USA). The chemical shifts were given in δ (ppm), and coupling constants were reported in Hz. HR-MS spectra were obtained on a JEOL JMS-700 instrument (Tokyo, Japan). Column chromatography (CC) was carried out on polyamide 6L and Sephadex LH 20. Precoated silica gel plates (Merck, Kieselgel 60 F_{254}, 0.25 mm, Merck, Darmstadt, Germany) and precoated RP-18 F_{254S} plates (Merck, Darmstadt, Germany) were used for TLC analysis. A semi-preparative reversed-phase column (Supelco C18 column 250 × 10 mm, 5 μm) was used for HPLC.

Plant material

Aerial parts of *P. arabica* (L.) DC., 1813 were collected from the Mediterranean coastal belt at Gamsa City, Al-Dakahlia Governorate, Egypt (31°26′35.4″N 31°33′35.5″E), during the flowering stage in April–May 2016. The Associate Professor of Taxonomy Dr Ahmed M. Abdel Gawad, Mansoura University, Egypt, collected and authenticated the plant material with a voucher specimen (PARA-016-978).

Extraction and purification

Following our previous protocol,[50] a black gum (75.6 g) of *P. arabica* dry material (850 g) was further chromatographed using silica gel column chromatography eluted with a mixture of $CHCl_3$/MeOH step gradient. Eight major fractions (PA 1-8) were afforded after the final collection, according to the TLC profile.

The elution of fraction PA-4 (1.18 g) over silica gel CC afforded **4** (68.7 mg) and **14** (11.3 mg) along with the subfraction PA-4A-B. The subfraction PA-4B (106.5 mg) was chromatographed on Sephadex LH-20 eluted with $CHCl_3$/MeOH (1 : 1) as the solvent system, and afforded **5** (9.8 mg) and **6** (13.6 mg). The subfraction PA-4A (82.6 mg) was eluted by $CHCl_3$/MeOH (1 : 1) over Sephadex LH-20, and afforded **7** (11.9 mg), **8** (17.2 mg) and **9** (10.5 mg). The fraction PA-5 (1.32 g) was chromatographed on silica gel CC and eluted with a $CHCl_3$/MeOH step gradient, and afforded **10** (18.3 mg), **11** (9.2 mg), and the subfraction PA-5A-B. The chromatography of subfraction PA-5B (43.2 mg) over Sephadex LH-20 using $CHCl_3$/MeOH (1 : 1) as the elution solvent afforded **12** (15.1 mg). The fraction PA-6 (796.4 mg) was chromatographed over ODS-C18 CC using H_2O/MeOH in order of increasing polarity as the eluent, and afforded subfraction PA-6A-C. Subfraction PA-6B (72.1 mg) was subjected to RP-18 HPLC (MeOH–H_2O, 3.5 : 6.5) and afforded **1** (7.3 mg), **2** (5.4 mg) and **13** (16.5 mg). Subfraction PA-6C (19.6 mg) was eluted by $CHCl_3$/MeOH (1 : 1) over Sephadex LH-20 and afforded **3** (3.4 mg).

Spectroscopic data of compounds 1–3

Paronychiarabicine A (1):. Yellow amorphous powder; [α] −5.1 (C 0.1, MeOH); TOF-ESI-MS 559.1924 $[M + Na]^+$, (calc.: 559.1944; $C_{30}H_{32}O_9Na$); FT-IR at 3346, 2958, 1723, 1320, 1234, 1187 and 1037 cm^{-1}; for ^{1}H and ^{13}C NMR data (500 MHz, MeOH) see Table 1.

Paronychiarabicine B (2). Yellow amorphous powder; [α] −15.6 (C 0.1, MeOH), LR-CIMS *m*/*z* 536 $(M)^+$, HR-CIMS 536.2030 $[M]^+$, (calc.: 536.2046; $C_{30}H_{32}O_9$); FT-IR at 3343, 2961, 2318, 1725, 1297, 1205 and 1121 cm^{-1}; for ^{1}H and ^{13}C NMR data (500 MHz, MeOH) see Table 1.

Paronychiarabicastigmane A (3). White amorphous powder; [α] −6.6 (C 0.1, MeOH), (+)-FAB-MS *m*/*z* 537 $[M + H])^+$, (+)-LR-FAB-MS *m*/*z* 559 $[M + Na]^+$, HR-FAB-MS at *m*/*z* 559.2157 $[M + 1]^+$, (calc.: 559.2155; $C_{27}H_{36}O_{11}Na$); FT-IR at 3416, 2964, 1723, 1320, 1234, 1187 and 1037 cm^{-1}; for ^{1}H and ^{13}C NMR data (500 MHz, MeOH) see Table 2.

Acid hydrolysis of 3

Two milligrams of **3** in 1 ml 2% H_2SO_4 solution was heated under reflux for 2 h, then the reaction mixture was dried followed by dissolving in distilled H_2O and neutralizing with NaOH. The neutralized mixture was tested with some sugar moieties such as glucose, rhamnose and others using numerous elution systems over silica gel TLC.[32,33,51]

TDDFT-simulated ECD calculations

To simulate the circular dichroism (ECD) spectra, a conformational analysis was first carried out to generated all possible conformations of compounds **1–3** using Omega2 software.[52] The generated conformations within the energy window value of 10 kcal mol^{-1} were optimized at the B3LYP/6-31G* level of theory, followed by frequency calculations to estimate the Gibbs free energies. Time-dependent density functional theory (TDDFT) calculations with incorporating a polarizable continuum model (PCM) using methanol as a solvent were performed at the B3LYP/6-31+G* level of theory to calculate the

first fifty excitation states. SpecDis 1.71 was used to generate ECD spectra for the investigated compounds.[53] Gaussian band shapes with a sigma value of 0.20–30 ev were applied for ECD spectra generation. The generated ECD spectra were Boltzmann-averaged. All quantum mechanical calculations were performed using Gaussian09 software.[54]

Molecular docking

The crystal structures of the SARS-CoV-2 main protease (M^{pro}; PDB code: 6LU7,[55] papain-like protease (PL^{pro}; PDB code: 6W9C [56] and RNA-dependent RNA polymerase (RdRp; PDB code: 6M71 [57] were taken as templates for the molecular docking calculations. The docking calculations were carried out using AutoDock4.2.6 software[58] according to our previously described protocol, against SARS-CoV-2 targets.[49,58,59] The AutoDock protocol was followed to prepare the pdbqt files for the three investigated SARS-CoV-2 targets.[60] For the three SARS-CoV-2 targets, the binding site was realized by a docking box around the active site with XYZ dimensions of 60 Å × 60 Å × 60 Å and a spacing value of 0.375 Å. The atomic charges of the isolated compounds were assigned using the Gasteiger method.[61] The built-in clustering analysis with 1.0 Å RMSD tolerance was utilized to process the predicted binding positions.

Target prediction and pathway enrichment analysis (PEA)

For the pathway enrichment, we initially predicted all of the biological targets for megastigmane (**3**) as a SARS-CoV-2 inhibitor using the SwissTargetPredicition online tool (http://www.swisstargetprediction.ch). The DisGeNET database (https://www.disgenet.org) was used to collect the available information on human gene–disease associations (GDAs) for SARS diseases. The protein–protein interaction (PPI) network was developed using the STRING database for the top 20 predicted gene targets.[62] To investigate all possible target–function relations based on the network profiles, pathway enrichment analysis was performed for the top 20 SARS diseases-related genes using Cytoscape software V.3.8.2.[63] Finally, the Cytoscape-based ReactomeFIViz tool was integrated to visualize and model all possible drug–target interactions.[64]

Conclusion

The chemical characterization of the aerial parts of *P. arabica* led to the isolation and identification of two novel oxetane containing lignans, paronychiarabicine A (**1**) and B (**2**), one new megastigmane, paronychiarabicastigmane A (**3**), in addition to eleven known metabolites. The absolute configurations of the new compounds were achieved based on NOESY experiments as well as experimental and TDDFT-calculated electronic circular dichroism. Molecular docking calculations demonstrated the competitive binding affinity of the isolated compound **3** as a prospective SARS-CoV-2 M^{pro} inhibitor.

Conflicts of interest

The authors declare that there are no conflicts of interest.

Acknowledgements

Dr Elshamy gratefully acknowledges the subsidy from the Takeda Science Foundation, Japan. Additionally, this work was supported by the Tokushima Bunri University, Japan and the National Research Centre, Egypt. The computational work was completed with resources supported by the Science and Technology Development Fund, STDF, Egypt, grant nos 5480 & 7972 (granted to Dr Mahmoud A. A. Ibrahim). Prof. Mohamed Hegazy acknowledges the financial support from the Alexander von Humboldt Foundation "Georg Foster Research Fellowship for Experienced Researchers". The National Research Centre, Egypt is gratefully acknowledged.

References

1 M. K. Cheung, G. G. L. Yue, P. W. Y. Chiu and C. B. San Lau, *Front. Pharmacol.*, 2020, **11**, 744.
2 B. Adhikari, B. P. Marasini, B. Rayamajhee, B. R. Bhattarai, G. Lamichhane, K. Khadayat, A. Adhikari, S. Khanal and N. Parajuli, *Phytother. Res.*, 2021, **35**, 1298–1312.
3 J. C. Boulos, M. Rahama, M.-E. F. Hegazy and T. Efferth, *Cancer Lett.*, 2019, **459**, 248–267.
4 U. Anand, N. Jacobo-Herrera, A. Altemimi and N. Lakhssassi, *Metabolites*, 2019, **9**, 258.
5 D. H. Eroğlu, D. Altay and Ü. Budak, *International Journal of Secondary Metabolite*, 2017, **4**, 103–107.
6 F. U. Afifi, B. Al-Khalidi and E. Khalil, *J. Ethnopharmacol.*, 2005, **100**, 314–318.
7 S. Bouanani, C. Henchiri, E. Migianu-Griffoni, N. Aouf and M. Lecouvey, *J. Ethnopharmacol.*, 2010, **129**, 38–45.
8 M. P. B. De Santayana and E. Morales, *J. Ethnopharmacol.*, 2005, **98**, 1–19; *J. Ethnopharmacol.*, 2005, **98**, 1.
9 A. Ferreira, C. Proença, M. L. Serralheiro and M. E. Araújo, *J. Ethnopharmacol.*, 2006, **108**, 31–37.
10 D. Gülcemal, M. Masullo, Ö. Alankuş-Çalışkan and S. Piacente, *Fitoterapia*, 2014, **92**, 274–279.
11 S. Sait, S. Hamri-Zeghichi, L. Boulekbache-Makhlouf, K. Madani, P. Rigou, V. Brighenti, F. Pio Prencipe, S. Benvenuti and F. Pellati, *J. Pharm. Biomed. Anal.*, 2015, **111**, 231–240.
12 D. M. Zama, Z. Tebibel, W. Benayssa, F. Benayache, S. Benayache and A. Vlietinck, *Indian J. Pharmacol.*, 2007, **39**, 145–150.
13 S. Avunduk, O. Alankuş-Calişkan, T. Miyamoto, C. Tanaka and M. A. Lacaille-Dubois, *Nat. Prod. Commun.*, 2011, **6**, 205–208.
14 S. Avunduk, M. A. Lacaille-Dubois, T. Miyamoto, E. Bedir, S. G. Senol and O. A. Calişkan, *J. Nat. Prod.*, 2007, **70**, 1830–1833.
15 A. Braca, A. Bader, T. Siciliano and N. De Tommasi, *Magn. Reson. Chem.*, 2008, **46**, 88–93.

16 M. Curini, F. Epifano, L. Menghini and R. Pagiotti, *Chem. Nat. Compd.*, 2004, **40**, 190–191.
17 N. Zhu, D. Zhang, W. Wang, X. Li, B. Yang, J. Song, X. Zhao, B. Huang, W. Shi, R. Lu, P. Niu, F. Zhan, X. Ma, D. Wang, W. Xu, G. Wu, G. F. Gao, W. Tan, I. China Novel Coronavirus and T. Research, *N. Engl. J. Med.*, 2020, **382**, 727–733.
18 A. I. Elshamy, T. A. Mohamed, M. M. Marzouk, T. A. Hussien, A. Umeyama, M. E. F. Hegazy and T. Efferth, *Phytochem. Lett.*, 2018, **24**, 105–109.
19 A. A. Ahmed, M. E. F. Hegazy, N. M. Hassan, M. Wojcinska, J. Karchesy, P. W. Pare and T. J. Mabry, *Phytochemistry*, 2006, **67**, 1547–1553.
20 M.-E. F. Hegazy, T. A. Mohamed, A. I. Elshamy, A. A. Hassanien, N. S. Abdel-Azim, M. A. Shreadah, I. I. Abdelgawad, E. M. Elkady and P. W. Pare, *Nat. Prod. Res.*, 2016, **30**, 340–344.
21 T. A. Mohamed, A. I. Elshamy, A. R. Hamed, K. A. Shams and M. E. F. Hegazy, *Phytochem. Lett.*, 2018, **28**, 32–36.
22 M.-E. F. Hegazy, T. A. Mohamed, F. F. Abdel-Latif, M. S. Alsaid, A. A. Shahat and P. W. Pare, *Phytochem. Lett.*, 2013, **6**, 383–386.
23 T. Hirata, A. Takarada, M.-E. F. Hegazy, Y. Sato, A. Matsushima, Y. Kondo, A. Matsuki and H. Hamada, *J. Mol. Catal. B: Enzym.*, 2005, **32**, 131–134.
24 A. Bezerianos, A. Dragomir and P. Balomenos, in *Computational Methods for Processing and Analysis of Biological Pathways*, Springer, 2017, pp. 11–46.
25 H. Lee and M. Shin, *BioData Min.*, 2017, **10**, 3.
26 P. Y. P. Kao, K. H. Leung, L. W. C. Chan, S. P. Yip and M. K. H. Yap, *Biochim. Biophys. Acta, Gen. Subj.*, 2017, **1861**, 335–353.
27 S. Haider, C. Q. Yao, V. S. Sabine, M. Grzadkowski, V. Stimper, M. H. W. Starmans, J. Wang, F. Nguyen, N. C. Moon and X. Lin, *Nat. Commun.*, 2018, **9**, 4746.
28 S. A. G. Fleming and J. J. Gao, *Tetrahedron Lett.*, 1997, **38**, 5407–5410.
29 S. Saphier, Y. Hu, S. C. Sinha, K. N. Houk and E. Keinan, *J. Am. Chem. Soc.*, 2005, **127**, 132–145.
30 S. N. Sulaiman, A. Zahari, S. Y. Liew, M. Litaudon, A. M. Issam, H. A. Wahab and K. Awang, *Phytochem. Lett.*, 2018, **25**, 22–26.
31 K. Gao, D. Ma, Y. Cheng, X. Tian, Y. Lu, X. Du, H. Tang and J. Chen, *J. Agric. Food Chem.*, 2015, **63**, 1067–1075.
32 A. I. Elshamy, T. A. Mohamed, S. L. Al-Rowaily, A. M. Abd-ElGawad, B. A. Dar, A. A. Shahat and M. F. Hegazy, *Molecules*, 2019, **24**, 2412.
33 K. Wei, W. Li, K. Koike, L. Liu, X. Fu, L. Lin, Y. Chen and T. Nikaido, *Chem. Pharm. Bull.*, 2004, **52**, 776–779.
34 N. Matsuda and M. Kikuchi, *Chem. Pharm. Bull.*, 1996, **44**(9), 1676–1679.
35 Y. S. Wang, Z. Liao, Y. Li, R. Huang, H. B. Zhang and J. H. Yang, *J. Braz. Chem. Soc.*, 2011, **22**, 2234–2238.
36 M. M. A. Rahman, P. M. Dewick, D. E. Jackson and J. A. Lucas, *Phytochemistry*, 1990, **29**, 1971–1980.
37 N. P. Thao, B. T. Luyen, J. E. Koo, S. Kim, Y. S. Koh, N. V. Thanh, N. X. Cuong, P. V. Kiem, C. V. Minh and Y. H. Kim, *Pharm. Biol.*, 2016, **54**, 588–594.
38 X. Wang, C. Zhang, Y. Peng, H. Zhang, Z. Wang, Y. Gao, Y. Liu and H. Zhang, *Food Chem.*, 2018, **246**, 41–47.
39 J. Zhang, S. Yamada, E. Ogihara, M. Kurita, N. Banno, W. Qu, F. Feng and T. Akihisa, *Chem. Biodiversity*, 2016, **13**, 1601–1609.
40 T. T. Guo, X.-F. Tang, J. Chang and Y. Wang, *Nat. Prod. Res.*, 2017, **31**, 16–21.
41 H. Zhang, N. Feng, Y. T. Xu, T. X. Li, X. M. Gao, Y. Zhu, Y. S. Song, Y. N. Wang and H. H. Wu, *Chem. Biodiversity*, 2017, **14**, e1600437.
42 Y. Yang, Y. B. Yang, W. Q. Lu, Z. J. Wu and W. S. Chen, *Chem. Nat. Compd.*, 2017, **53**, 417–421.
43 Y. J. Kuo, S. Y. Hwang, M. D. Wu, C. C. Liao, Y. H. Liang, Y. H. Kuo and H. O. Ho, *Chem. Pharm. Bull.*, 2008, **56**, 585–588.
44 A. Pauli and K. H. Kubeczka, *Nat. Prod. Commun.*, 2010, **5**, 1387–1394.
45 S. H. García B., F. Navarro, J. Pedro and D. Lazari, *Phytochemistry*, 1996, **41**, 1113–1117.
46 R. Vitek, L. M. R. de Novais, H. F. V. Torquato, E. J. Paredes-Gamero, M. G. de Carvalho, P. T. de Sousa Jr, M. J. Jacinto and V. C. da Silva, *Nat. Prod. Res.*, 2017, **31**, 1930–1934.
47 S. Zúñiga, J. L. Cruz, I. Sola, P. A. Mateos-Gómez, L. Palacio and L. Enjuanes, *J. Virol.*, 2010, **84**, 2169–2175.
48 C.-H. Wu, S.-H. Yeh, Y.-G. Tsay, Y.-H. Shieh, C.-L. Kao, Y.-S. Chen, S.-H. Wang, T.-J. Kuo, D.-S. Chen and P.-J. Chen, *J. Biol. Chem.*, 2009, **284**, 5229–5239.
49 G. M. Morris, R. Huey, W. Lindstrom, M. F. Sanner, R. K. Belew, D. S. Goodsell and A. J. Olson, *J. Comput. Chem.*, 2009, **30**, 2785–2791.
50 A. I. Elshamy, T. A. Mohamed, M. Suenaga, M. Noji, A. Umeyama, T. Efferth and M.-E. F. Hegazy, *Phytochem. Lett.*, 2019, **34**, 74–78.
51 C. A. Seo, E.-K. Ahn, J.-S. Kang, J.-H. Leeb, J. S. Oh and S. Hong, *Phytochem. Lett.*, 2017, **20**, 93–97.
52 P. C. Hawkins, A. G. Skillman, G. L. Warren, B. A. Ellingson and M. T. Stahl, *J. Chem. Inf. Model.*, 2010, **50**, 572–584.
53 T. Bruhn, A. Schaumlöffel, Y. Hemberger and G. Bringmann, *Chirality*, 2013, **25**, 243–249.
54 M. J. Frisch, G. W. Trucks, H. B. Schlegel, G. E. Scuseria, M. A. Robb, J. R. Cheeseman, G. Scalmani, V. Barone, B. Mennucci, G. A. Petersson, H. Nakatsuji, M. Caricato, X. Li, H. P. Hratchian, A. F. Izmaylov, J. Bloino, G. Zheng, J. L. Sonnenberg, M. Hada, M. Ehara, K. Toyota, R. Fukuda, J. Hasegawa, M. Ishida, T. Nakajima, Y. Honda, O. Kitao, H. Nakai, T. Vreven, J. A. Montgomery, J. E. Peralta, F. Ogliaro, M. Bearpark, J. J. Heyd, E. Brothers, K. N. Kudin, V. N. Staroverov, R. Kobayashi, J. Normand, K. Raghavachari, A. Rendell, J. C. Burant, S. S. Iyengar, J. Tomasi, M. Cossi, N. Rega, J. M. Millam, M. Klene, J. E. Knox, J. B. Cross, V. Bakken, C. Adamo, J. Jaramillo, R. Gomperts, R. E. Stratmann, O. Yazyev, A. J. Austin, R. Cammi, C. Pomelli, J. W. Ochterski, R. L. Martin, K. Morokuma, V. G. Zakrzewski, G. A. Voth,

P. Salvador, J. J. Dannenberg, S. Dapprich, A. D. Daniels, Ö. Farkas, J. B. Foresman, J. V. Ortiz, J. Cioslowski and D. J. Fox, *Gaussian 09 Revision E01*, Gaussian Inc., Wallingford CT, USA, 2009.

55 Z. Jin, X. Du, Y. Xu, Y. Deng, M. Liu, Y. Zhao, B. Zhang, X. Li, L. Zhang, C. Peng, Y. Duan, J. Yu, L. Wang, K. Yang, F. Liu, R. Jiang, X. Yang, T. You, X. Liu, X. Yang, F. Bai, H. Liu, X. Liu, L. W. Guddat, W. Xu, G. Xiao, C. Qin, Z. Shi, H. Jiang, Z. Rao and H. Yang, *Nature*, 2020, **582**, 289–293.

56 J. Osipiuk, S. A. Azizi and S. Dvorkin, *Nat. Commun.*, 2021, **12**, 743.

57 Y. Gao, L. Yan, Y. Huang, F. Liu, Y. Zhao, L. Cao, T. Wang, Q. Sun, Z. Ming, L. Zhang, J. Ge, L. Zheng, Y. Zhang, H. Wang, Y. Zhu, C. Zhu, T. Hu, T. Hua, B. Zhang, X. Yang, J. Li, H. Yang, Z. Liu, W. Xu, L. W. Guddat, Q. Wang, Z. Lou and Z. Rao, *Science*, 2020, **368**, 779–782.

58 T. A. Mohamed, A. I. Elshamy, M. A. Ibrahim, A. Zellagui, M. F. Moustafa, A. H. Abdelrahman, S. Ohta, P. W. Pare, M.-E. F. Hegazy, T. A. Mohamed, A. I. Elshamy, M. A. Ibrahim, A. Zellagui, M. F. Moustafa, A. H. Abdelrahman, S. Ohta, P. W. Pare and M.-E. F. Hegazy, *RSC Adv.*, 2020, **10**, 34541–34548.

59 M. A. A. Ibrahim, A. H. M. Abdelrahman, T. A. Hussien, E. A. A. Badr, T. A. Mohamed, H. R. El-Seedi, P. W. Pare, T. Efferth and M.-E. F. Hegazy, *Nucleic Acids Res.*, 2020, **126**, 104046.

60 S. Forli, R. Huey, M. E. Pique, M. F. Sanner, D. S. Goodsell and A. J. Olson, *Nat. Protoc.*, 2016, **11**, 905–919.

61 J. Gasteiger and M. Marsili, *Tetrahedron*, 1980, **36**, 3219–3228.

62 H. V. Cook, N. T. Doncheva, D. Szklarczyk, C. Von Mering and L. J. Jensen, *Viruses*, 2018, **10**, 519.

63 P. Shannon, A. Markiel, O. Ozier, N. S. Baliga, J. T. Wang, D. Ramage, N. Amin, B. Schwikowski and T. Ideker, *Genome Res.*, 2003, **13**, 2498–2504.

64 A. S. Blucher, S. K. McWeeney, L. Stein and G. Wu, *F1000Researh*, 2019, **8**, 908.